Chemical Science

ROYAL SOCIETY OF CHEMISTRY

EDGE ARTICLE

View Article Online
View Journal | View Issue

Cite this: *Chem. Sci.*, 2026, **17**, 9516

All publication charges for this article have been paid for by the Royal Society of Chemistry

Received 4th November 2025
Accepted 24th March 2026

DOI: 10.1039/d5sc08545d

rsc.li/chemical-science

Resonator-based add-drop filters enabled by flexible polymorphic crystals with TADF-RTP motifs

Pradip Pattanayak, †[a] Ankur Khapre,†[b] Shamim Ahmad,[a] Avulu Vinod Kumar,[b] Bishes Ray,[a] Satendra Kumar,[a] Chilla Malla Reddy,[c] Rajadurai Chandrasekar*[b] and Pradipta Purkayastha *[a]

We demonstrate the use of yellow and green fluorescence (Y-FL and G-FL) obtained from polymorphic crystals as signals in an add-drop filter (P-ADF). This innovation leverages two distinct crystalline polymorphs, green (G) and yellow (Y), of 5′-(9-ethyl-9*H*-carbazol-3-yl)-[2,2′-bithiophene]-5-carbaldehyde (CZ-CHO), which exhibit RTP and TADF, respectively. The differing emissive behaviors are attributed to unique intermolecular interactions and crystal packing in each polymorph, which also provide mechanical flexibility. A functional optical circuit, comprising two Y-FL and one G-FL crystal waveguides, is constructed utilizing an AFM-tip-based micromanipulation technique. The circuit configuration enables the G-FL signal emitted from the waveguide to be modulated and transduced into a Y-FL output. Remarkably, the circular shape of the single crystal acts as a ring resonator, and allows for clockwise or anticlockwise signal routing. Our findings establish a new paradigm for polymorph-driven photonic circuit design and open avenues for tunable signal processing using TADF/RTP emissive materials.

Introduction

Flexible materials are gaining significant attention as they offer solutions to the limitations of rigid, silicon-based technologies. While soft materials like polymers and composites have been widely studied due to their defect-free and structurally ordered nature, flexible organic crystals have recently emerged as a compelling alternative.[1–6] These crystals uniquely combine mechanical flexibility with desirable optoelectronic characteristics, making them promising candidates for the next generation of advanced technologies, such as optical waveguides,[7–9] optical modulators,[10] micro-interferometers,[11] photonic integrated circuits (PICs),[12–14] visible light communication devices,[15–18] lasers,[19–21] *etc.* This newfound flexibility opened the door to a wide range of applications, particularly in fields where traditional materials like polymers, elastomers, and liquid crystals have long dominated.[22–30] One of the most exciting aspects of organic molecular crystals is their ability to undergo reversible mechanical bending,[31–37] offering a form of elasticity that has significant potential in various technologies. Depending on their specific response to external forces, these crystals can exhibit different behaviours, such as elastic (reversible bending),[38–41] plastic (irreversible bending),[42–46] and pseudo-plastic (irreversible bending on a substrate)[11–14,47] properties, which have made them attractive alternatives to more conventional materials, providing a lightweight and versatile option for applications that demand flexibility and resilience. Organic crystals with high quantum yields (QYs), emission brightness, colour purity, and photo-stability,[48–52] are increasingly being explored for their potency in fabricating photonic devices. Specifically, crystals with thermally activated delayed fluorescence (TADF) and room-temperature phosphorescence (RTP) properties are highly sought after. These materials are unique in their ability to efficiently capture 100% of radiative transitions, a feature that makes them ideal for using in optoelectronic devices.[53–55] TADF and RTP represent two advanced photophysical processes through which organic crystals can enhance the efficiency of light emission. In RTP, the molecule undergoes intersystem crossing (ISC) from the first singlet excited state (S_1) to a triplet excited state (T_n), followed by vibrational cascade (VC) and radiative transition from the first triplet state (T_1) to the ground state (S_0).[56–59] In contrast, TADF involves a thermally assisted reverse intersystem crossing (RISC) from near-degenerate T_1 back to S_1, enabling efficient light emission with enhanced brightness.[60–62] These molecular photophysical processes were extensively used for the development of organic light-emitting diodes (OLEDs),[63–66] and organic field-effect transistors (OFETs),[67–69] however, not yet applied for crystal based PIC components.

---

[a] *Department of Chemical Sciences and Centre for Advanced Functional Materials, Indian Institute of Science Education and Research (IISER) Kolkata, Mohanpur 741246, West Bengal, India. E-mail: ppurkayastha@iiserkol.ac.in*

[b] *Advanced Photonic Materials and Technology Laboratory, School of Chemistry and Centre for Nanotechnology, University of Hyderabad, Prof. C. R. Rao Road, Hyderabad 500046, Telangana, India. E-mail: r.chandrasekar@uohyd.ac.in*

[c] *Department of Chemistry, Indian Institute of Technology Hyderabad, Hyderabad, 502285, Telangana, India*

† These authors have contributed equally.

Among various photonic elements, waveguides and resonators play a crucial role by confining, enhancing, and steering optical signals in desired paths.[11–14,70–73] Ring resonators (RRs), in particular, are widely utilized in functions like bandwidth filtering, add-drop filtering, racetrack resonators, and other PIC applications.[11–14,74–78] Photonic add-drop filters (ADF) are essential components in PICs.[71–73,79] Structurally, an ADF typically comprises an RR, which is a "looped waveguide" coupled with one or two "bus waveguides". When laterally coupled with two parallel waveguides, the RR can direct light in either a clockwise or counterclockwise path providing an opportunity to control the light path within the circuit. However, the fabrication of TADF and RTP-based ADF remains challenging, as it requires the integration of optically and mechanically distinct organic single crystals on a substrate.

Herein, we report the first demonstration of optical signal interconversion between TADF and RTP within a polymorphic add-drop filter (P-ADF). Two polymorphic green (G) and yellow (Y) emissive crystalline forms of 5'-(9-ethyl-9*H*-carbazol-3-yl)-[2,2′-bithiophene]-5-carbaldehyde (CZ-CHO) exhibit RTP and TADF, respectively. Mechanical flexibility in both the polymorphs is governed by favourable intermolecular interactions within their respective crystal structures. A mechanical micromanipulation technique based on atomic force microscopy (AFM) cantilever tip known as mechanophotonics,[12–14] has been employed to construct a P-ADF using optical waveguides composed of two Y crystals and one G crystal. In the P-ADF, the G-waveguide transduces the fluorescence signal into Y-FL waveguide through light splitting and colour modulation. The input-position dependent investigation of clockwise or counterclockwise light routing in P-ADF facilitates singlet–singlet interconversion. This approach lays the groundwork for the integration of polymorphic crystals into next-generation photonic circuit technologies (Scheme 1).

Results and discussion

Designing a suitable organic small molecule to serve the desired objective is the key challenge in device applications. We thoughtfully chalked out CZ-CHO, our model TADF molecule, to achieve a clear difference between the HOMO and the LUMO. We incorporated an *N*-ethyl carbazole (CZ) unit as the donor motif (D), ensuring localization of an electron-rich wavefunction to it. Addition of an ethyl group to the nitrogen atom in CZ was a deliberate strategy to enhance the mechanical flexibility within the crystal structure.[80,81] Building on our earlier findings, we selected a single bond connected bithiophene unit as the π-spacer to promote polymorphism during crystallization (Fig. S3A).[80] The robust D–π–A structure was successfully synthesized through a one-step Suzuki–Miyaura coupling reaction in 75% yield (Scheme S1). CZ-CHO was purified by column chromatography and checked by ^{1}H, ^{13}C NMR spectroscopy and HRMS (Fig. S1–S3).

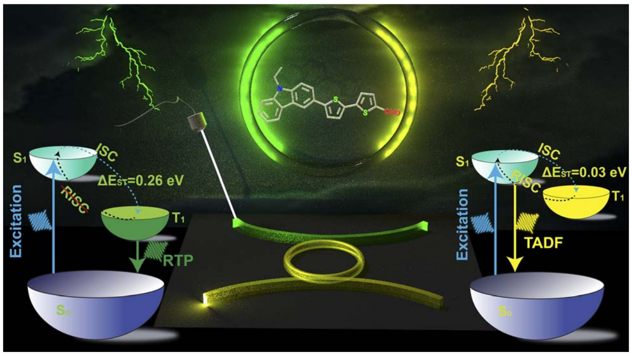

Scheme 1 Illustration of the approach employed to capture the interplay between RTP and TADF through mechanically flexible polymorphic crystal waveguides made from CZ-CHO.

Polymorphism in CZ-CHO and preparation of microcrystals

Molecular self-assembly follows either the thermodynamic or kinetic pathway (Fig. 1A). In general, the stable thermodynamic product is favoured because the kinetic aggregates spontaneously reorganize toward the thermodynamically equilibrium state through thermal movements in the molecules. Unfortunately, thermodynamic self-assembly of dyes often suffers from severe emission quenching due to dense molecular packing.[82] Moreover, the kinetically controlled intermolecular interactions successfully led to the development of polymorphed single-crystals. We have used a temperature-steered molecular self-assembling strategy to synthesize the thermodynamic and kinetic macrocrystals with different intermolecular interactions from the same CZ-CHO molecule (Fig. 1B), which is difficult but achievable under careful observation. In the thermodynamically stable dye macrocrystals, small intermolecular distances correspond to strong intermolecular π–π interactions inducing intermolecular charge-transfer (Inter-CT) and excimer emission with low quantum efficiency that ceases the lasing capability. In contrast, the kinetically formed dye macrocrystals, with large intermolecular distances and weak intermolecular interactions, support highly efficient intramolecular charge-transfer (Intra-CT) driven monomeric emission. The CZ-CHO crystals, obtained under kinetic and thermodynamic control, are shown in Fig. 1C and D, respectively. The powder X-ray diffraction (PXRD) patterns from these crystals initially confirmed the polymorphism (Fig. S4). Furthermore, growth of the CZ-CHO polymorphic crystals could be controlled by varying the precursor concentration, which precisely adjusted the size. Significantly brighter emission from the ends of the crystalline CZ-CHO wires compared to that from the body, as demonstrated in Fig. 1C and D, exhibits the typical features of active optical waveguide. Smooth surface of the microwires reduce optical scattering loss and infuse them with exceptional optical waveguide characteristics. Most crucially, the kinetically and thermodynamically obtained CZ-CHO crystals emit green (G) and yellow (Y) lights with 65.2% and 48.7% photoluminescence quantum yield (PLQY), due to different chemical packing modes in the polymorphic crystals.

Microcrystals, due to their reduced dimensions, exhibit pseudo-plasticity that aids in circuit fabrication enabling light confinement and manipulation. Whereas, the larger size of the

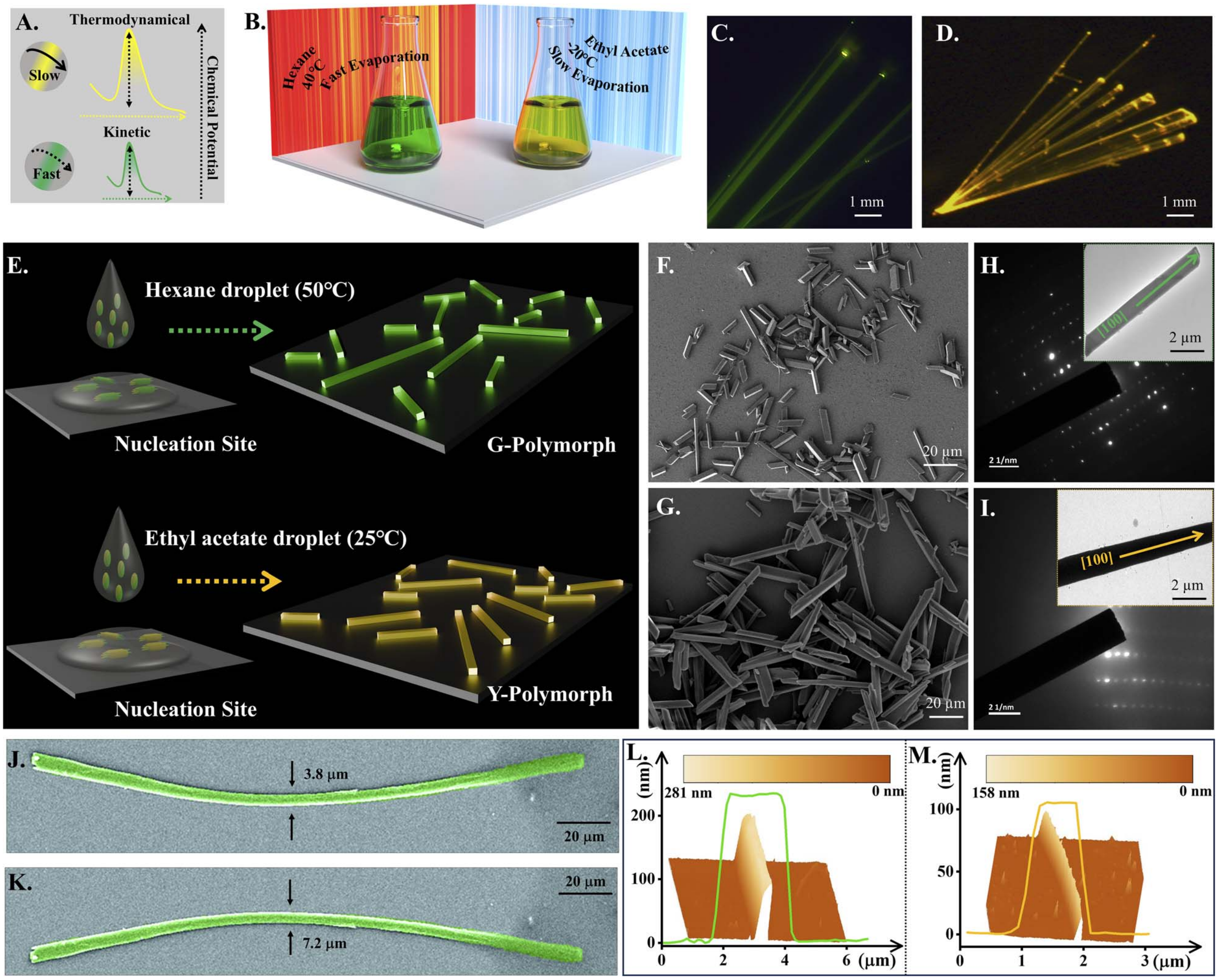

Fig. 1 Illustrations of (A and B) development of the thermodynamically and kinetically controllable single crystals from CZ-CHO; PL microscopy images of the CZ-CHO macrocrystals under kinetic (C) and thermodynamic control (D); (E) schematic illustration of crystallization technique to get the polymorphic microcrystals; (F and G) SEM photographs, (H and I) the SAED patterns, (J and K) the false coloured SEM images (bended) and (L and M) the 3D AFM images of the G and Y microcrystals, respectively. The insets of H and I show the corresponding TEM images of the 1D microcrystals.

macrocrystals may lead to defect-induced scattering, resulting in signal loss during light propagation. On the other hand, microcrystals typically possess fewer defects and imperfections compared to macrocrystals, leading to more efficient signal transmission with minimum loss. To synthesize high-quality polymorphic microcrystals from CZ-CHO, saturated solutions of CZ-CHO were prepared in hexane and ethyl acetate at high (50 °C) and, low (25 °C) temperatures, respectively, as shown in Fig. 1E. Nucleation and growth of the CZ-CHO polymorphic microcrystals was initiated by dropping the two precursor solutions separately onto glass substrates at 25 °C followed by solvent evaporation to get densely packed crystal nuclei that further stimulated molecular growth resulting thermodynamically stable single-crystals. The hotter precursor droplets, on the other hand, on cooling and evaporation, led to rapid molecular nucleation promoting the formation of loosely packed crystal nuclei leading to the kinetic single-crystal products. Scanning electron microscope (SEM) images (Fig. 1F and G) confirmed the smooth morphology of the 1D G and Y crystalline microrods. The PXRD peaks and bright selected area electron diffraction (SAED) patterns suggested crystallinity of the sample (Fig. 1H and I). Surprisingly, we observed that the synthesized microcrystals could be bent up to several microns without any micro manipulation indicating their flexibility (Fig. 1J and K). Heights of the two polymorphic crystals, obtained from the three-dimensional (3D) AFM topography, were 100 and 200 nm, respectively, for the Y (Fig. 1M) and the G crystals (Fig. 1L). These results demonstrate that a controlled solution-evaporation technique can effectively be used to grow polymorphic microcrystals.

Crystal structure analysis

As mentioned before, CZ-CHO crystallized into two distinct elastically bendable polymorphic forms, G (CCDC NO: 2484035) and Y (CCDC NO: 2484038) (Fig. 2A and B). The detailed

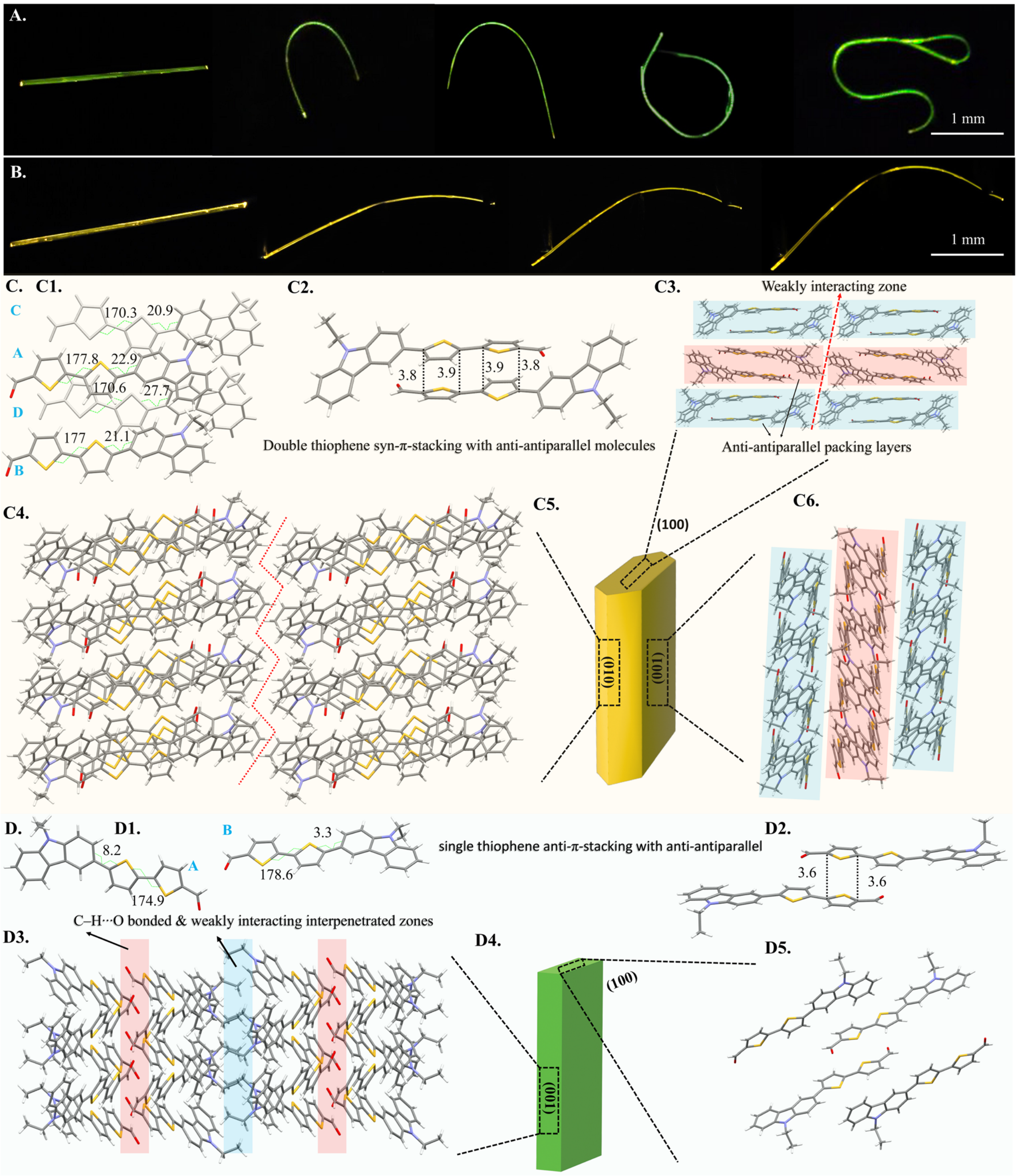

Fig. 2 Fluorescence microscopy images of the bendable (A) G and (B) Y crystals under UV light; view of the crystal packing view from different faces of the Y (C) and the G (D) crystals; (C1) asymmetric unit consisting of four molecules, (C2) double thiophene syn-π-stacking between anti-parallel molecules, (C3, C4 and C6) crystal packing along the (100), (010) and (001), respectively of the Y crystal; (D1) the G crystals consist of two molecules in the asymmetric unit, (D2) single thiophene anti-π-stacking between anti-parallel molecules, and D3 and D5 represent crystal packing view from the (001) and (100) planes, respectively of the G crystal (D4).

crystallographic parameters are provided in Table S1. The Y form crystallizes in triclinic $P\bar{1}$ space group consisting four molecules in the asymmetric unit (Fig. 2C1). Extending the crystal packing revealed a bifurcated hydrogen bonding of the O atom of the –CHO group with a single centre. The unit cell has eight molecules with thiophene units positioned opposite to each other at dihedral angles (θ) ranging from 170.3° to 177.8° (Fig. 2C1). Furthermore, the out-of-plane thiophene and benzyl moieties exhibit dihedral angle of more than 20°. The Y crystals also form a dimer with anti-parallel molecular configuration resulting into double thiophene π–π syn-stacking (Fig. 2C2). The molecules are packed in anti-parallel A–B–A layers with weakly interacting dispersive zones (shown by a dotted red arrow in Fig. 2C3). The crystals displayed significant reversible (elastic) bendability on exposing to three-point bending, which allowed them to curl into loops along the main plane (001) with a maximum elastic strain of 11.64%. Viewing along the 'b' axis (perpendicular to the (001) plane) exposed a molecular interlocking zigzag pattern serving as a buffer for the reversible bend (Fig. 2C4). Similarly, the G form is packed with a triclinic $P\bar{1}$ space group with just two molecules (Fig. 2D1) in the asymmetric unit, with the unit cell consisting of four molecules. Furthermore, each 'O' atom in the –CHO groups formed an intermolecular bifurcated hydrogen connection with distinct molecules. The molecules form supramolecular dimers with a single thiophene anti-π-stacking between the antiparallel molecules (Fig. 2D2). The dihedral angles (θ) exhibit greater planarity in G compared to Y, with 170° and 178.6° angles between the anti-parallel thiophenes, and 3.3° and 8.2° between the thiophene and benzyl units (Fig. 2D1). Qualitative three-point mechanical bending experiments demonstrated that the crystals could bend elastically into loops on applying force perpendicular (⊥) to the major plane (010), with a maximum elastic strain of 5.57%. Packing of the minor face (001) exposes alternating interpenetrated C–H–O hydrogen-bonded and weakly interacting zones (Fig. 2D3), which apparently contribute to the massive reversible elastic bending of the G crystals.

Regulation of TADF and RTP in the polymorphic microcrystals

Both the G and Y polymorphic forms exhibit red shifted optical absorption band compared to that in the solution state (Fig. S5). Moreover, these microcrystals show excitation wavelength independent behaviour (Fig. 3A and B). Such a red shift in the absorption spectrum in the solid state typically occurs due to J aggregation.[83] The G microcrystals showed bi-modal emission on excitation at 405 nm with the emission maxima at 545 and 580 nm. These G and Y polymorphs have respective average fluorescence lifetimes of 2.62 and 4.76 ns (Fig. S6). Moreover, a 1 ms delay resulted a new emission band at 600 nm (Fig. 3E), when the fluorescence band was totally quenched on applying a high time gate. This established that the 600 nm band is attributed to RTP. We used time-gated PL and temperature-dependent phosphorescence decay to further validate the existence of the triplet exciton. The 600 nm band exhibits a high lifespan of 3.25 ms at ambient temperature, which rises with a temperature drop and eventually reaches 7.98 ms at 78 K (Fig. 3F). RTP in the G microcrystals was amply demonstrated by the delayed PL intensity increase under cryogenic condition (Fig. 3G). The typical electronic transition scheme, as ascribed from the experimental observations, is given in Fig. 3C as calculated from Fig. S8A. The Y microcrystals produced a broad emission band with $\lambda_{\max}$ of 565 nm when excited at 405 nm. Interestingly, the delayed (gated) spectrum resembled the prompt (20 µs delay time), hinting triplet exciton harvesting *via* thermally assisted RISC (Fig. 3H). Lifespan of the delayed fluorescence at 298 K was 5.75 µs, which decreased to 2.68 µs at 78 K (Fig. 3I). Drop in the delayed fluorescence intensity at 78 K further validated the effective RISC at room temperature and supported the formation of TADF from the Y crystals (Fig. 3J). Fig. 3D and S8B portray the energy profile of the Y crystals, and Table S2 and Fig. S7 depict the photophysical insights of both the polymorphs. The calculated phosphorescence lifetime of the Y crystals is 30.25 ms at 78 K (Fig. S8C).

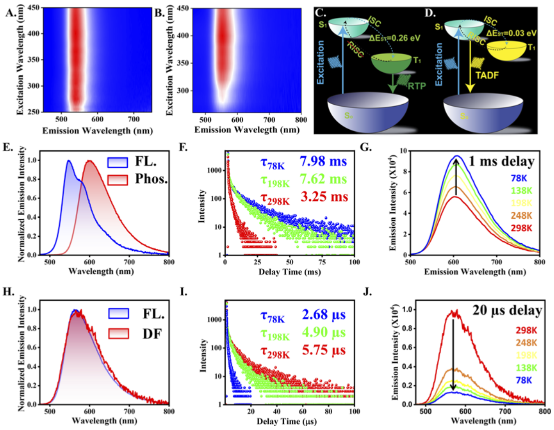

Fig. 3 (A and B) Excitation–emission fluorescence maps; (C and D) the energy level diagrams portraying RTP and TADF of the G and Y microcrystals; (E) prompt fluorescence and phosphorescence (1 ms delay time) spectra recorded at room temperature; (F and G) the temperature dependent PL decays and the gated PL of the G green microcrystals; (H) the prompt and delayed fluorescence (20 µs delay time) spectra, and (I and J) the temperature-dependent PL decay and gated PL of the Y microcrystals.

Mechanical properties of the crystals

Both the polymorphs exhibit highly reversible mechanical flexibility, as demonstrated by three-point bending tests (Fig. 4A and B). The mechanical properties for both the crystalline forms were quantified using nanoindentation by applying 3 and 5 mN stress on the main faces of the single crystals (Fig. 4C). The elastic modulus (E: resistance to elastic deformation) and hardness (H: resistance to plastic deformation) were obtained using a Berkovich tip in a load control mode from the Oliver-Pharr method analysing the load (P)–displacement (h) curves.[84] On indenting the major face (001) of the Y form, E and H were found to be 3.38 ± 0.13 GPa and 130.74 ± 10.12 MPa at 5 mN (Fig. 4F3, F4, S9 and S10), which had the respective average contact depths of 1212.95 ± 46.16 nm and 868.90 ± 131.97 nm (Table S3). Conversely, mechanical characteristics of the G microcrystals are somewhat higher but not significantly different. At 5 mN load, the average E was 3.63 ± 0.17 GPa and the average H was 146.98 ± 8.73 MPa (Fig. 4G1 and 4G2). Fig. 4G3 and 4G4 show the contact depth (hc) to be 1142.03 ± 34.46 nm upon indentation. The 3D post indentation impression and statistical distribution of E and H are also shown in Fig. 4F2 and 6G2, whereas, plots for the mechanical property parameters are provided in the SI for the 3 mN load for both the forms (Fig. S11 and S12). Absence of sudden noticeable displacement bursts (or pop-ins) in the P-h curves during the loading segment for both the forms is an indication of smooth penetration of the indenter tip due to homogeneous response against the external mechanical stress. Besides, no trace of pile-up after the indent impression suggests their compressible nature. Slightly higher modulus and H for the G crystals suggest better deformation recovery capacity and resistance to the plastic deformation. Indentation on the major face (001) of the

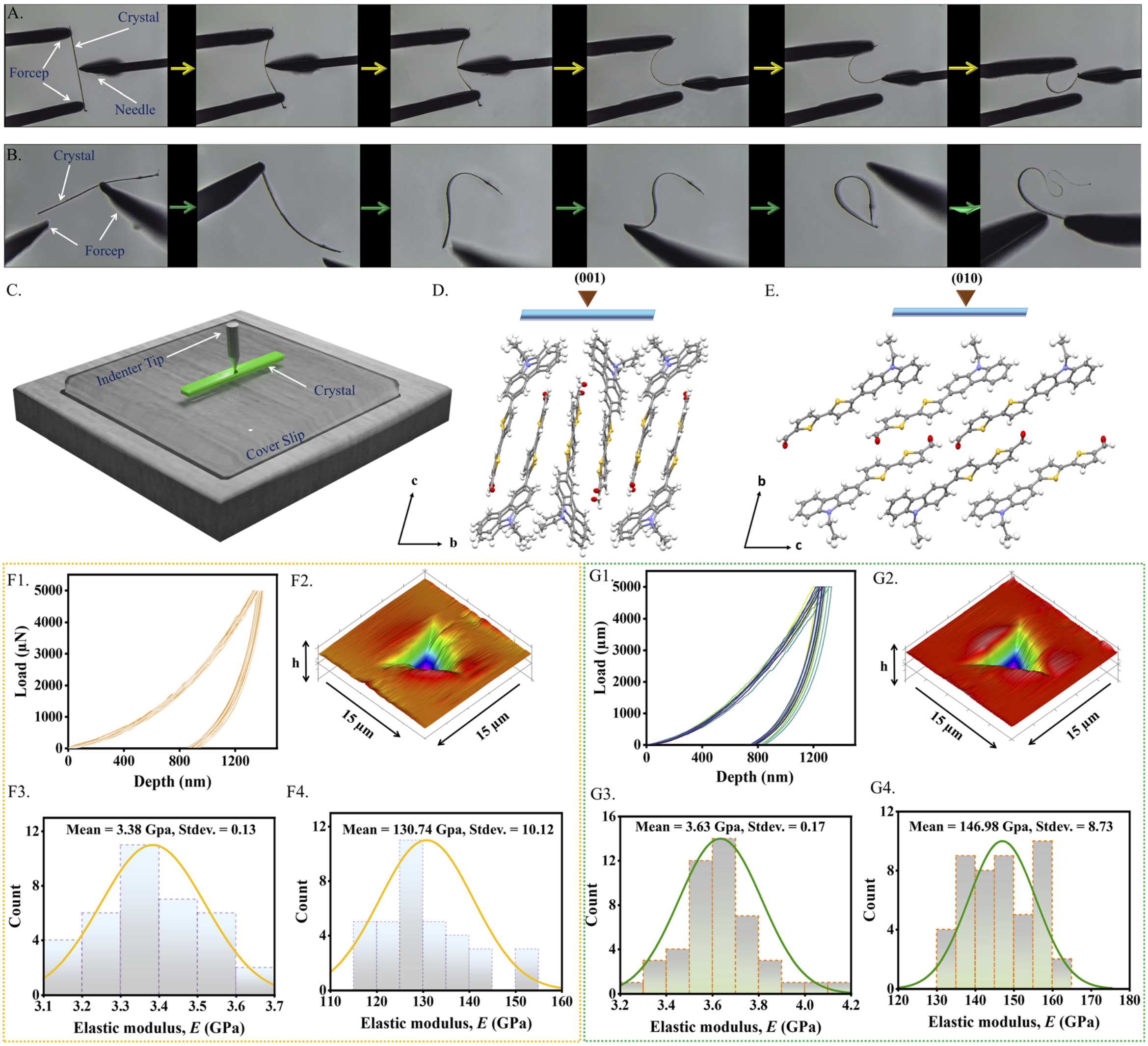

Fig. 4 Illustration of mechanical elastic bendability of the (A) Y and (B) G crystals; (C) schematic representation of the nanoindentation setup; (D and E) crystal packing from the side face while indenting on the major face of the Y (001) and G (010) forms, respectively; (F) NI plots for the Y form at 5 mN; (F1) multiple load (P)–displacement (h) curves; (F2) 3D post impression of the indentation caters; (F3 and F4) histogram plots for the elastic modulus and hardness with their respective values; (G) NI plots for the G crystal at 5 mN; (G1) multiple load P-h curves; (G2) 3D indentation impression from the SPM imaging, and (G3 and G4) the histogram plots for the elastic modulus and hardness, respectively.

Y crystals causes the tip to penetrate relatively parallel to the molecular layers inferring a slightly softer nature.

Circuit fabrication and optical waveguiding studies

A confocal microscope equipped with an AFM was used to perform the single-particle micro-PL and mechanophotonic analyses of the polymorphic crystals. The G and Y polymorphs of CZ-CHO were obtained by employing different growth conditions in ethyl acetate : hexane mixtures at 1 : 3 and 3 : 1 ratio during self-assembly. Based on their photophysical properties, the Y-polymorph exhibits TADF, while the G-polymorph demonstrates RTP, each with distinct mechanical properties. Exploiting these mechanical characteristics, a reconfigurable photonic circuit was fabricated using TADF and RTP polymorphic crystals. Typically, the tip of TADF-active Y polymorph (OW-1; length $L \approx 320$ μm and thickness $T \approx 600$ nm) was excited with a focused 405 nm laser, and the resulting yellow emission ($\lambda_{\max} \sim 580$ nm) was recorded at the opposite tip of the waveguide. The PL detected at the distal tip of OW-1 resembled that recorded at the excitation point, albeit with slight bandwidth narrowing in the higher-energy region due to molecular reabsorption. Notably, the reabsorbed spectrum featured discrete optical modes in the PL emission, attributed to back-and-forth reflection of trapped light between the mirror-like facets of OW-1 crystal (Fig. S13). The PL intensity (I) decreased with increasing optical path length (D), as the active distance between excitation and detection points grew. The optical loss of $\alpha \approx 0.0765$ dB μm^{-1} for the waveguide was determined by fitting the following equation.

$$\frac{I_{\text{tip}}}{I_{\text{body}}} = \mathrm{e}^{-\alpha D}$$

To assess the micro-mechanical compliance of OW-1, mechanical force was applied using the tip of an AFM cantilever on the crystal terminal end. The microcrystal underwent mechanical deformation along the direction of the applied force. However, unlike millimetre-sized crystals, the microcrystals retain their geometry in the stressed-state even after the withdrawal of AFM tip, demonstrating pseudo-plastic behaviour of OW-1 microcrystals. This pseudo-plasticity was further utilized to construct a ring resonator (RR) from straight OW-1 crystal *via* extreme micromechanical bending, resulting in a TADF-based RR (Fig. 5A, B and S14). The RR exhibited optical waveguiding properties comparable to its parent straight waveguide, OW-1. Subsequently, another TADF-active waveguide, OW-2 ($L \approx 331$ μm and $T \approx 766$ nm), was mechanically integrated into the RR to fabricate a monolithic flexible organic photonic integrated circuit-1 (FOPIC-1) (Fig. 5E and S15). To develop a hybrid P-ADF, G-polymorphic waveguide of CZ-CHO was selected. Initially, a self-assembled G microcrystal, OW-3 with $L \approx 311$ μm and $T \approx 1.4$ μm, was illuminated with a focused laser beam, to observe a PL with dual $\lambda_{\max}$ centred at 545 nm and 580 nm (Fig. 5C). Optical modes were observed depending on the surface morphology of the microcrystals. The optical loss for OW-3 was 0.1127 dBμm^{-1}. Finally, OW-3 was micromechanically transferred and integrated with FOPIC-1 to realize a P-ADF (Fig. 5E(vii–viii) and S16). The mechanical flexibility of the G, Y microcrystal was demonstrated by bending the tips of OW-3 away from the RR to create a curvature, thereby effectively enhancing the evanescent coupling between the RR and OW-3 (Fig. 5F).

The hybrid P-ADF consists of four distinct ports, labelled T1 to T4: the first two ports are located in the G-fluorescence (G-FL) waveguide (OW-3), while the other two are in the Y-fluorescence (Y-FL) waveguide (OW-2) (Fig. 6A and B). The optical performance of the P-ADF was evaluated by analysing its PL output at various ports for a given laser input. The photonic response of the hybrid P-ADF is influenced by the energy transfer between the polymorphic waveguides; without this interaction, the circuit would only support a single optical bandwidth in the structure. Initially, the 405 nm laser light was introduced to port P1 in the OW-3 of the constructed P-ADF to induce G-FL in the waveguide, which then transduces and outcouple at port P2. At the junction between OW-3 and the RR, the G-FL actively couples resulting into two optical bandwidths in the circuit, corresponding to both G-FL and Y-FL. This occurred due to the energy transfer from the G-FL waveguide to the RR, which enabled optical excitation of Y-FL and its clockwise signal circulation. Further, the Y-FL signal passively propagates inside the OW-2 (Y-FL waveguide); and outcouples at T3, while there is no optical signal flow towards port T4 (Fig. 6C). Similarly, when the laser was introduced at the T2 port, the G-FL propagated towards T1 in the same waveguide. Further, the G-FL signal also enters into RR *via* evanescent field coupling. The signal converts into Y-FL *via* energy transfer and propagates in the counter-clockwise direction in RR and the modified Y-FL signal passively couples to the OW-2 in such a way that only T4 shows the output, not T3 (Fig. 6D).

Finally, port T3 of the OW-2 was excited by a 405 nm laser to generate TADF, which transduces to the other port of the same waveguide and outcoupled at T4. At the junction between OW-2 and RR, Y-FL passively couples into RR and recirculates in the resonator. This circulating passive optical signal evanescently couples into the adjacent waveguide OW-3, and the same signal

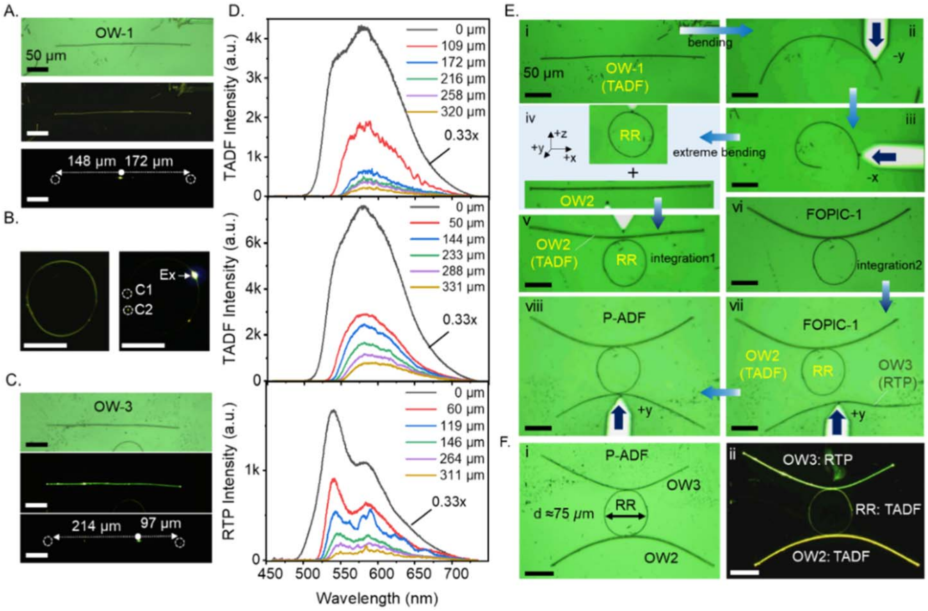

Fig. 5 Confocal microscopy bright field (top), FL (mid) and laser excited FL (bottom) images of (A) OW1 (yellow (Y) polymorph of CZ-CHO), (B) OW2 (Y polymorph of CZ-CHO), and (C) OW3, (green (G) polymorph of CZ-CHO), respectively; (D) position dependent PL spectra of OW1 (top) OW2 (middle) and OW3 (bottom), respectively; (E) confocal optical microscope images show the steps involved in the fabrication of ADF, (i–iv) optical images show the fabrication of RR from OW1, (v–vi) optical images show the fabrication of FOPIC-1 from OW2 and RR, (vii–viii) optical images show the fabrication of H-ADF from FOPIC-1 and OW3; (F) confocal microscopy (i) bright field and (ii) FL images of H-ADF, respectively.

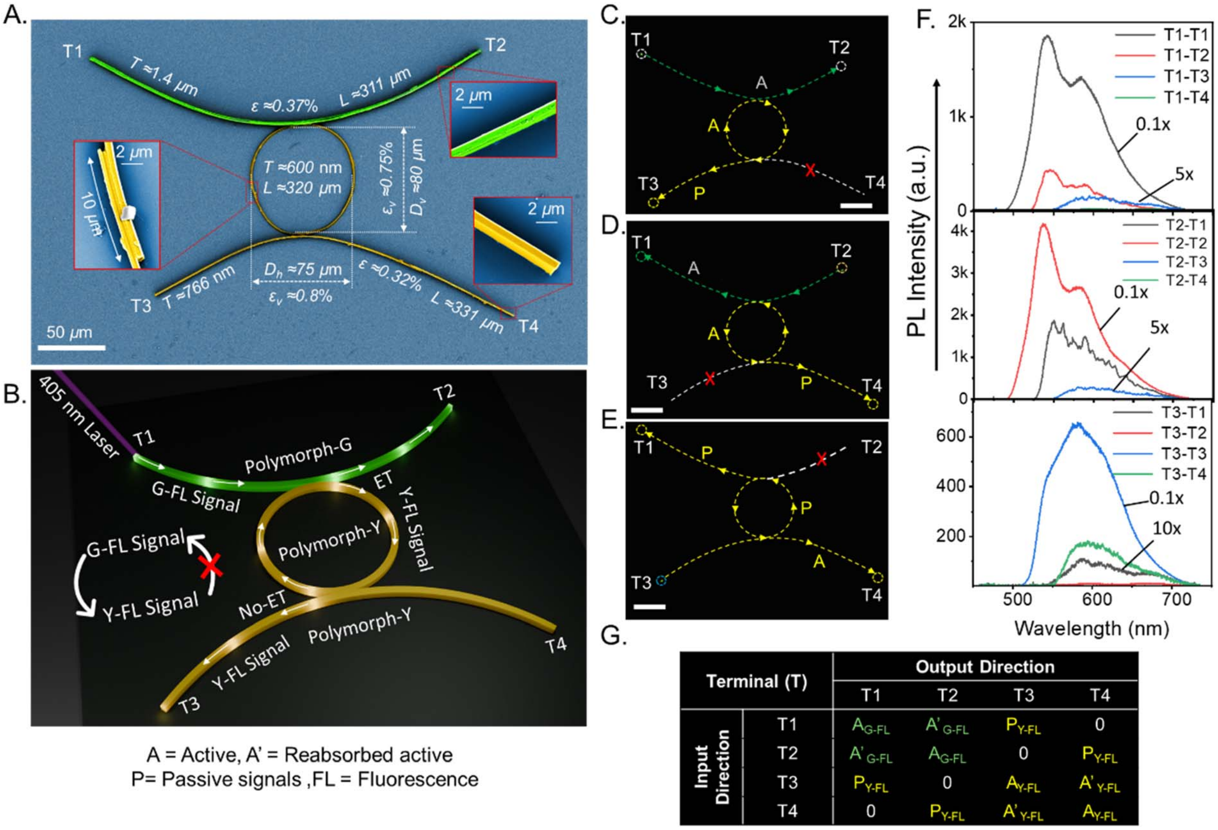

Terminal (T)		Output Direction			
		T1	T2	T3	T4
Input Direction	T1	$A_{G\text{-}FL}$	$A'_{G\text{-}FL}$	$P_{Y\text{-}FL}$	0
	T2	$A'_{G\text{-}FL}$	$A_{G\text{-}FL}$	0	$P_{Y\text{-}FL}$
	T3	$P_{Y\text{-}FL}$	0	$A_{Y\text{-}FL}$	$A'_{Y\text{-}FL}$
	T4	0	$P_{Y\text{-}FL}$	$A'_{Y\text{-}FL}$	$A_{Y\text{-}FL}$

A = Active, A′ = Reabsorbed active
P= Passive signals ,FL = Fluorescence

Fig. 6 (A) Color-coded FESEM image shows the geometric information of the H-ADF (left, right top and right bottom insets show the precisely attached tips of the Y-polymorph ring, surface of the G-polymorph waveguide, and the tip of the Y-polymorph waveguide, respectively); (B) schematic of the H-ADF showing active and passive signal propagation; (C–E) the dark field confocal images showing the circuits for each terminal excitation and the collection at all four positions (scale bar: 50 μm); (F) the corresponding PL spectra for each excitation, and (G) input-dependent directional specific optical outputs obtained in the fabricated optical component.

propagates towards port T1 as there is no possibility of energy transfer from Y-FL to G-FL waveguides. However, as determined by the circuit design, no optical signal flows toward port T2 (Fig. 6E). The contrasting photophysical properties of the polymorphic waveguides thereby enrich the circuit with diverse optical functionalities, depending on the attributes of each waveguide. Fig. 6F shows the corresponding PL spectra for each excitation and Fig. 6G provides the input-dependent directional specific optical outputs obtained in the fabricated optical component.

Conclusions

This study presented an important advancement in organic photonic circuit device engineering through the first successful demonstration of optical signal interconversion between Y-FL and G-FL. Utilizing the polymorphic nature of the organic emitter CZ-CHO, two distinct flexible crystalline forms were isolated and designated as G and Y exhibiting RTP and TADF emissions, respectively. The divergent emissive behaviour arises from differences in the molecular packing and intermolecular interactions, which not only define their photophysical properties but also impart mechanical flexibility, enabling precise structural manipulation. Using the mechanophotonics technique, a P-ADF circuit, composed of three integrated waveguides: two Y-crystals exhibiting yellow TADF and one G-crystal displaying red RTP, was fabricated. This circuit configuration allowed dynamic signal transduction in which G-FL, generated in the G-waveguide, was modulated and split into Y-FL emissions *via* coupling with the Y waveguides. Remarkably, the system also permits directional control of signal propagation either clockwise or counter-clockwise, based on the input light, highlighting the programmable nature of the interconversion process. The ability to engineer and manipulate singlet–singlet transitions within a reconfigurable photonic ADF marks a significant milestone in organic photonics. This approach not only offers a new degree of freedom in the design of all-organic photonic circuits but also establishes a foundational framework integrating switchable emissive states into next-generation optical logic systems, sensors, and quantum photonic platforms.

Author contributions

Pradip Pattanayak: investigation, methodology, data curation, writing – original draft, review and editing. Ankur Khapre: investigation, methodology, data curation, writing – original draft, review and editing. Shamim Ahmad: investigation, data curation. Avulu Vinod Kumar: investigation, data curation. Bishes Ray: investigation, data curation. Satendra Kumar: investigation, data curation. Chilla Malla Reddy: investigation, review and editing. Rajadurai Chandrasekar: investigation, methodology, writing – original draft, review and editing. Pradipta Purkayastha: supervision, conceptualization, writing – review & editing, funding acquisition.

Conflicts of interest

There are no conflicts to declare.

Data availability

The data supporting this article have been included as part of the supplementary information (SI). Supplementary information: [detailed experimental section, supporting figures and tables]. See DOI: https://doi.org/10.1039/d5sc08545d.

CCDC 2484035[85a] and 2484038[85b] contain the supplementary crystallographic data for this paper.

Acknowledgements

PP acknowledges the financial support from the Anusandhan National Research Foundation (ANRF) through the project CRG/022/000006 and IISER Kolkata for the infrastructure. RC acknowledges ANRF [SERBSTR/2022/00011 and CRG/2023/003911] for financial support. P. Pattanayak and SK acknowledge the University Grants Commission (UGC), Government of India and the Council of Scientific and Industrial Research (CSIR), New Delhi, for their fellowship.

Notes and references

1 W. M Awad, D. W Davies, D. Kitagawa, J. M. Halabi, M. B Al-Handawi, I. Tahir, F. Tong, G. Campillo-Alvarado, A. G. Shtukenberg, T. Alkhidir, Y. Hagiwara, M. Almehairbi, L. Lan, S. Hasebe, D. P. Karothu, S. Mohamed, H. Koshima, S. Kobatake, Y. Diao, R. Chandrasekar, H. Zhang, C. C. Sun, C. Bardeen, R. O. Al-Kaysi, B. Kahr and P. Naumov, *Chem. Soc. Rev.*, 2024, **52**, 3098–3169.

2 H. Liu, Z. Lu, Z. Zhang, Y. Wang and H. Zhang, *Angew. Chem., Int. Ed.*, 2018, **57**, 8448.

3 M. Rohullah, V. Vinay Pradeep, S. Singh and R. Chandrasekar, *Nat. Commun.*, 2024, **15**, 4040.

4 X. Yang, L. Lan, L. Li, X. Liu, P. Naumov and H. Zhang, *Nat. Commun.*, 2022, **13**, 2322.

5 X. Yang, L. Lan, X. Pan, Q. Di, X. Liu, L. Li, P. Naumov and H. Zhang, *Nat. Commun.*, 2023, **14**, 2287.

6 Q. Lv, M. Zheng, X. Wang and L. Liao, *Small*, 2022, **18**, 2203961.

7 L. Lan, L. Li, P. Naumov and H. Zhang, *Chem. Mater.*, 2023, **35**, 7363–7385.

8 P. Naumov, D. P. Karothu, E. Ahmed, L. Catalano, P. Commins, J. M. Halabi, M. B. Al-Handawi and L. Li, *J. Am. Chem. Soc.*, 2020, **142**, 13256–13272.

9 L. Lan and H. Zhang, *Angew. Chem., Int. Ed.*, 2024, **63**, e202411405.

10 D. Venkatakrishnarao, M. A. Mohiddon, N. Chandrasekhar and R. Chandrasekar, *Adv. Opt. Mater.*, 2015, **3**, 1035–1040.

11 J. Ravi, M. Annadhasan, A. Vinod Kumar and R. Chandrasekar, *Adv. Funct. Mater.*, 2021, **31**, 2100642.

12 R. Chandrasekar, *Small*, 2021, **17**, 2100277.

13 R. Chandrasekar, *Adv. Opt. Mater.*, 2023, **11**, 2301124.

14 R. Chandrasekar, *Chem. Commun.*, 2022, **58**, 3415.

15 A. Khapre, A. V. Kumar and R. Chandrasekar, *Laser Photonics Rev.*, 2024, **19**, 2400278.

16 A. Vinod Kumar, M. Rohullah, M. Chosenyah, J. Ravi, U. Venkataramudu and R. Chandrasekar, *Angew. Chem., Int. Ed.*, 2023, **62**, e202300046.

17 A. V. Kumar, M. Godumala, J. Ravi and R. Chandrasekar, *Angew. Chem., Int. Ed.*, 2022, **134**, e202212382.

18 A. Khapre, J. Hazarika and R. Chandrasekar, *Nat. Commun.*, 2025, **16**, 10862.

19 X. Zhang, H. Dong and W. Hu, *Adv. Mater.*, 2018, **30**, 1801048.

20 Y. Shi and X. Wang, *Adv. Funct. Mater.*, 2020, **31**, 2008149.

21 H. Fang, J. Yang, J. Feng, T. Yamao, S. Hotta and H. Sun, *Laser Photonics Rev.*, 2014, **9**, 128.

22 M. Karl, J. M. E. Glackin, M. Schubert, N. M. Kronenberg, G. A. Turnbull, I. D. W. Samuel and M. C. Gather, *Nat. Commun.*, 2018, **9**, 1525.

23 M. Xu, C. Wei, Y. Zhang, J. Chen, H. Li, J. Zhang, L. Sun, B. Liu, J. Lin, M. Yu, L. Xie and W. Huang, *Adv. Mater.*, 2023, **36**, 2301671.

24 X. Wu, W. Fu and H. Chen, *ACS Appl. Polym. Mater.*, 2022, **4**, 4609–4623.

25 K. Liu, Y. Jiang, Z. Bao and X. Yan, *CCS Chem.*, 2019, **1**, 431–447.

26 S. Basak, A. M. Mohiddon, M. Baumgarten, K. Muellen and R. Chandrasekar, *Sci. Rep.*, 2015, **5**, 8406.

27 Y. Zhang, Y. Chen, J.-Q. Li, S.-E. Liu and Y. Liu, *Adv. Sci.*, 2024, **11**, 2307777.

28 Y. Zhang, C. Ellingford, R. Zhang, J. Roscow, M. Hopkins, P. Keogh, T. McNally, C. Bowen and C. Wan, *Adv. Funct. Mater.*, 2019, **29**, 1808431.

29 Y. Ning, D.-B. Yang, S. Yang, Y. Zhang, J. G. Saven and C. B. Murray, *J. Am. Chem. Soc.*, 2025, **147**, 6332–6337.

30 H. K. Bisoyi and Q. Li, *Chem. Rev.*, 2021, **122**, 4887–4926.

31 S. Ghosh and C. M. Reddy, *Angew. Chem., Int. Ed.*, 2012, **51**, 10319–10323.

32 N. Chandrasekhar and R. Chandrasekar, *Angew. Chem., Int. Ed.*, 2012, **51**, 3556–3561.

33 Q. Di, M. B. Al-Handawi, L. Li, P. Naumov and H. Zhang, *Angew. Chem., Int. Ed.*, 2024, **63**, e202403914.

34 A. Worthy, A. Grosjean, M. C. Pfrunder, Y. Xu, C. Yan, G. Edwards, J. K. Clegg and J. C. McMurtrie, *Nat. Chem.*, 2018, **10**, 65–69.

35 X. Ding, C. Wei, L. Wang, J. Yang, W. Huang, Y. Chang, C. Ou, J. Lin and W. Huang, *Smart Mater.*, 2023, **5**, e1213.

36 J. M. Halabi, E. Ahmed, L. Catalano, D. P. Karothu, R. Rezgui and P. Naumov, *J. Am. Chem. Soc.*, 2019, **141**, 14966–14970.

37 B. Tang, X. Yu, K. Ye and H. Zhang, *Adv. Opt. Mater.*, 2021, **10**, 2101335.

38 R. Huang, C. Wang, Y. Wang and H. Zhang, *Adv. Mater.*, 2018, **30**, 1800814.

39 H. Liu, Z. Lu, B. Tang, C. Qu, Z. Zhang and H. Zhang, *Angew. Chem., Int. Ed.*, 2020, **59**, 12944–12950.

40 S. Hayashi, S. Yamamoto, D. Takeuchi, Y. Ie and K. Takagi, *Angew. Chem., Int. Ed.*, 2018, **57**, 17002–17008.

41 J. Song, Y. Zhou, Z. Pan, Y. Hu, Z. He, H. Tian and X. Ma, *Matter*, 2023, **6**, 2005–2018.

42 S. Takamizawa, Y. Takasaki, T. Sasak and N. Ozaki, *Nat. Commun.*, 2018, **9**, 3984.

43 L. Catalano, D. P. Karothu, S. Schramm, E. Ahmed, R. Rezgui, T. J. Barber, A. Famulari and P. Naumov, *Angew. Chem., Int. Ed.*, 2018, **57**, 17254–17258.

44 H. Liu, Z. Bian, Q. Cheng, L. Lan, Y. Wang and H. Zhang, *Chem. Sci.*, 2018, **10**, 227–232.

45 J. Ravi, T. Feiler, A. Mondal, A. a. L. Michalchuk, C. M. Reddy, B. Bhattacharya, F. Emmerling and R. Chandrasekar, *Adv. Opt. Mater.*, 2022, **11**, 2201518.

46 S. Bhandary, A. J. Thompson, J. C. McMurtrie, J. K. Clegg, P. Ghosh, S. R. N. K. Mangalampalli, S. Takamizawa and D. Chopra, *Chem. Commun.*, 2020, **56**, 12841–12844.

47 M. Annadhasan, A. R. Agrawal, S. Bhunia, V. V. Pradeep, S. S. Zade, C. M. Reddy and R. Chandrasekar, *Angew. Chem., Int. Ed.*, 2020, **59**, 13852–13858.

48 J. Song, L. Ma, S. Sun, H. Tian and X. Ma, *Angew. Chem., Int. Ed.*, 2022, **61**, e202206157.

49 P. Pattanayak, A. Nandi and P. Purkayastha, *Chem. Mater.*, 2023, **35**, 9799–9805.

50 H. Uoyama, K. Goushi, K. Shizu, H. Nomura and C. Adachi, *Nature*, 2012, **492**, 234–238.

51 S. Li, L. Fu, X. Xiao, H. Geng, Q. Liao, Y. Liao and H. Fu, *Angew. Chem., Int. Ed.*, 2021, **60**, 18059–18064.

52 J. Wang, Y. Yang, K. Li, L. Zhang and Z. Li, *Angew. Chem., Int. Ed.*, 2023, **62**, e202304020.

53 D. Barman, M. Annadhasan, A. P. Bidkar, P. Rajamalli, D. Barman, S. S. Ghosh, R. Chandrasekar and P. K. Iyer, *Nat. Commun.*, 2023, **14**, 6648.

54 J. Gierschner, J. Shi, B. M. Medina, D. R. Sanjuán, S. Varghese and S. Y. Park, *Adv. Opt. Mater.*, 2021, **9**, 2002251.

55 A. A. Dar and A. A. Malik, *J. Mater. Chem. C*, 2024, **12**, 9888–9913.

56 P. Pattanayak, A. Nandi, R. Patra and P. Purkayastha, *Adv. Opt. Mater.*, 2023, **12**, 2302155.

57 W. Zhao, Z. He, J. W. Y. Lam, Q. Peng, H. Ma, Z. Shuai, G. Bai, J. Hao and B. Z. Tang, *Chem*, 2016, **1**, 592–602.

58 J. Yang, Z. Ren, Z. Xie, Y. Liu, C. Wang, Y. Xie, Q. Peng, B. Xu, W. Tian, F. Zhang, Z. Chi, Q. Li and Z. Li, *Angew. Chem., Int. Ed.*, 2016, **56**, 880–884.

59 W. Zhao, Z. He and B. Z. Tang, *Nat. Rev. Mater.*, 2020, **5**, 869–885.

60 M. Godumala, A. V. Kumar and R. Chandrasekar, *J. Mater. Chem. C*, 2021, **40**, 14115.

61 P. Pattanayak, N. Modak, S. Guchhait, N. Ghosh and P. Purkayastha, *Adv. Opt. Mater.*, 2024, **12**, 2400404.

62 A. Chatterjee, J. Chatterjee, S. Sappati, R. Tanwar, M. D. Ambhore, H. Arfin, R. M. Umesh, M. Lahiri, P. Mandal and P. Hazra, *Chem. Sci.*, 2023, **14**, 13832–13841.

63 S. Reineke, F. Lindner, G. Schwartz, N. Seidler, K. Walzer, B. Lussem and K. Leo, *Nature*, 2009, **459**, 234–238.

64 J. Yang, Z. Wang, F. Wang, R. Xu, J. Tao, S. Zhang, Q. Qin, B. L. Davies, C. Jagadish, Z. Yu and Y. Lu, *Light Sci. Appl.*, 2016, **5**, e16046.

65 M. Schwarze, W. Tress, B. Beyer, F. Gao, R. Scholz, C. Poelking, K. Ortstein, A. A. Gunther, D. Kasemann, D. Andrienko and K. Leo, *Science*, 2016, **352**, 1446–1449.

66 Y. Wang, L. Sun, C. Wang, F. Yang, X. Ren, X. Zhang, H. Dong and W. Hu, *Chem. Soc. Rev.*, 2019, **48**, 1492–1530.

67 G. Zhao, H. Dong, Q. Liao, J. Jiang, Y. Luo, H. Fu and W. Hu, *Nat. Commun.*, 2018, **9**, 4790.

68 X. Wu, C. Gao, Q. Chen, Y. Yan, G. Zhang, T. Guo and H. Chen, *Nat. Commun.*, 2023, **14**, 1579.

69 D. P. Karothu, G. Dushaq, E. Ahmed, L. Catalano, M. Rasras and P. Naumov, *Angew. Chem., Int. Ed.*, 2021, **60**, 26151.

70 M. Lipson, *Nat. Mater.*, 2022, **21**, 974.

71 J. Ravi and R. Chandrasekar, *Adv. Opt. Mater.*, 2021, **9**, 2100550.

72 A. V. Kumar, E. Mamonov, T. Murzina and R. Chandrasekar, *Adv. Opt. Mater.*, 2022, **11**, 2201507.

73 J. Ravi, A. V. Kumar, D. P. Korathu, M. Annadhasan, P. Naumov and R. Chandrasekar, *Adv. Funct. Mater.*, 2021, **31**, 2105415.

74 N. Huby, D. Pluchon, N. Coulon, M. Belloul, A. Moreac, E. Gaviot, P. Panizza and B. Beche, *Opt. Commun.*, 2010, **283**, 2451.

75 V. V. Pradeep and R. Chandrasekar, *Adv. Opt. Mater.*, 2022, **10**, 2201150.

76 W. Zhang, J. Yao and Y. S. Zhao, *Acc. Chem. Res.*, 2016, **49**, 1691–1700.

77 F. Sasaki, S. Kobayashi, S. Haraichi, S. Fujiwara, K. B. Y. Masumoto and S. Hotta, *Adv. Mater.*, 2007, **19**, 3653.

78 H. Yoshioka, T. Ota, C. Chen, S. Ryu, K. Yasui and Y. Oki, *Sci. Rep.*, 2015, **5**, 10623.

79 A. V. Kumar and R. Chandrasekar, *Adv. Opt. Mater.*, 2023, **11**, 2201009.

80 A. V. Kumar, P. Pattanayak, A. Khapre, A. Nandi, P. Purkayastha and R. Chandrasekar, *Angew. Chem., Int. Ed.*, 2024, **63**, e202411054.

81 J. Mei, N. L. C. Leung, R. T. K. Kwok, J. W. Y. Lam and B. Z. Tang, *Chem. Rev.*, 2015, **115**, 11718–11940.

82 W. Dong, C. Zhang, H. Dong, Z. Zhou, J. Yao and Y. S. Zhao, *ACS Nano*, 2022, **16**, 12345–12351.

83 S. Wu, W. Zhang, C. Li, Z. Ni, W. Chen, L. Gai, J. Tian, Z. Guo and H. Lu, *Chem. Sci.*, 2024, **15**, 5973.

84 Y. Su, S. Bhunia, S. Xu, A. Chen, C. M. Reddy and T. Cai, *Chem. Mater.*, 2021, **33**, 4821–4829.

85 (*a*) CCDC 2484035: Experimental Crystal Structure Determination, 2026, DOI: 10.5517/ccdc.csd.cc2pcv53; (*b*) CCDC 2484038: Experimental Crystal Structure Determination, 2026, DOI: 10.5517/ccdc.csd.cc2pcv86.